Homogeneously dispersed, multimetal oxygen-evolving catalysts

Bo Zhang,[1,2]* Xueli Zheng,[1,3]* Oleksandr Voznyy,[1]* Riccardo Comin,[1] Michal Bajdich,[4,5] Max García-Melchor,[4,5] Lili Han,[3,6] Jixian Xu,[1] Min Liu,[1] Lirong Zheng,[7] F. Pelayo García de Arquer,[1] Cao Thang Dinh,[1] Fengjia Fan,[1] Mingjian Yuan,[1] Emre Yassitepe,[1] Ning Chen,[8] Tom Regier,[8] Pengfei Liu,[9] Yuhang Li,[9] Phil De Luna,[1] Alyf Janmohamed,[1] Huolin L. Xin,[6] Huagui Yang,[9] Aleksandra Vojvodic,[4,5]† Edward H. Sargent[1]†

[1]Department of Electrical and Computer Engineering, University of Toronto, 35 St George Street, Toronto, Ontario M5S 1A4, Canada. [2]Department of Physics, East China University of Science & Technology, 130 Meilong Road, Shanghai 200237, China. [3]Tianjin Key Laboratory of Composite and Functional Materials, School of Materials Science and Engineering, Tianjin University, Tianjin 300072, China. [4]SUNCAT Center for Interface Science and Catalysis, Department of Chemical Engineering, Stanford University, Stanford, CA 94305, USA. [5]SLAC National Accelerator Laboratory, 2575 Sand Hill Road, Menlo Park, CA 94025, USA. [6]Center for Functional Nanomaterials, Brookhaven National Laboratory, Upton, New York 11973, USA. [7]Beijing Synchrotron Radiation Facility, Institute of High Energy Physics, Chinese Academy of Sciences, Beijing 100049, China. [8]Canadian Light Source, Inc.(CLSI), 44 Innovation Boulevard, Saskatoon, SK, S7N 2V3, Canada. [9]Key Laboratory for Ultrafine Materials of Ministry of Education, School of Materials Science and Engineering, East China University of Science & Technology, 130 Meilong Road, Shanghai 200237, China.

*These authors contributed equally to this work

†Corresponding author. E-mail: ted.sargent@utoronto.ca (E.H.S); alevoj@stanford.edu (A.V.)

Earth-abundant first-row (3d) transition-metal-based catalysts have been developed for the oxygen-evolution reaction (OER); however, they operate at overpotentials significantly above thermodynamic requirements. Density functional theory suggested that non-3d high-valency metals such as tungsten can modulate 3d metal oxides, providing near-optimal adsorption energies for OER intermediates. We developed a room-temperature synthesis to produce gelled oxy-hydroxide materials with an atomically homogeneous metal distribution. These gelled FeCoW oxy-hydroxide exhibits the lowest overpotential (191 mV) reported at 10 mA per square centimeter in alkaline electrolyte. The catalyst shows no evidence of degradation following more than 500 hours of operation. X-ray absorption and computational studies reveal a synergistic interplay between W, Fe and Co in producing a favorable local coordination environment and electronic structure that enhance the energetics for OER.

Efficient, cost-effective and long-lived electrolysers are a crucial missing piece along the path to fuels synthesized with renewable electricity (*1*, *2*). The bottleneck in improving water-splitting technologies is the oxygen-evolving reaction (OER), where even the most efficient precious-metal catalysts require a substantial overpotential to reach the desired current densities $\geq$10 mA cm^{-2} (*2*, *3*). Researchers have explored earth-abundant first-row (3d) transition metal oxides (*4–9*), including 3d metal oxy-hydroxides (*4*, *5*), oxide perovskites (*7*), cobalt phosphate composites (*6*), nickel borate composites (*10*), and molecular complexes (*9*, *11*). The OER performance of multimetal oxides based on Fe, Co, and Ni is particularly promising, and OER activity often outperforms that of the corresponding single-metal oxides (*5*, *12–15*).

We examined whether multimetal oxide OER catalysts could be improved by systematically modulating their 3d electronic structure. Prior results suggest that the introduction of additional metals has a limited impact on the behavior of the 3d metals, likely because their undesired separation into two non-interacting metal oxide phases (*16*, *17*). For modulation, we focus in particular on W, which in

its highest oxidation state is a structurally versatile coordination host (*9*, *11*). We began with computational studies aimed at identifying effects of W-modulation of the local coordination environment; and the impacts on the resulting electronic structure and on the consequent energetics of the OER. The OER performance of unary Co, Fe and Ni oxides has been well established both from theory and experiment (*14*, *15*, *18*). Previous computational studies show that the OER activity is mainly driven by the energetics of the OER intermediates (*OH, *O, *OOH) on the surfaces, with the O to OH adsorption energy difference being the main descriptor for the observed activity trends among these materials (*14*, *15*, *18*). Binary metal oxides such as Ni-Fe and Co-Fe, as well as doped unary oxides, have also been investigated and their activity can also be predicted using the above-mentioned descriptor-based approach (*5*, *12*, *13*). Theoretical studies suggest that, for a given unary metal oxide, the energetics of OER intermediates can be modulated by incorporating metal elements, and that these tune thereby the catalytic activity of these materials.

Theoretical calculations of ternary and higher mixtures of oxides have been hindered by the complexity of these ma-

terials and the associated computational cost. We simplified our approach by starting from the calculated OER energetics for the pure β-CoOOH, γ-FeOOH and WO_3 phases; and estimating the effect of alloying on the energetics of OER intermediates via simple linear interpolation arguments. Calculations revealed that the adsorption energy of OH is too strong on the FeOOH(010) surface, while it is too weak on the CoOOH(01-12) and WO_3(001) surfaces (Fig. 1A) (19). To test the interpolation principle, we next calculated the OH adsorption energy on the Fe-doped CoOOH(01-12) surface: this energy falls approximately halfway between the one obtained for the unary CoOOH(01-12) and FeOOH(010) surfaces. Similarly, adding Co into WO_3(001) or adding W into CoOOH(01-12) led to an averaged OH adsorption energy for the $CoWO_4$ system (20) and W-doped CoOOH(01-12). By extending this scheme to ternary Co-Fe-W metal-oxide systems, we estimate that FeW-doped CoOOH(01-12) should result in near-optimal *OH energetics for OER.

Next, we performed DFT+U calculations of the energetics of all intermediates (*OH, *O, *OOH) and extracted overpotentials for the set of unary and Fe and W doped surfaces mentioned above (see computational methodology in Supplementary Material (19)). Given the plethora of possible ternary Co-Fe-W oxide alloys, we limited our computational study to the investigation of the above active site motifs, which are also expected to benefit from the interpolation scheme of Fig. 1A. We chose only to study the chemistry of substitutionally metal doped surface sites. All calculated theoretical OER overpotentials shown in the two-dimensional (2D) volcano plot of Fig. 1B support the general validity of the interpolation scheme not just for *OH energetics, but also notably for the O to OH adsorption energy difference, denoted as $\triangle G_O$-$\triangle G_{OH}$. The potential limiting kinetic barriers for the reaction were also experimentally determined (see below) and found to be small compared to thermodynamics (see Supplementary Materials (19)). The tunability of adsorption energies upon alloying would hence allow for significant improvement in OER activity.

We found that the OER activity of the unary pure CoOOH(01-12) surface can be improved via single-site doping with sub-surface Fe atoms. This improvement can be attributed to a change in $\triangle G_{OH}$ and also in $\triangle G_O$-$\triangle G_{OH}$ at the Co-site, and can be rationalized by the difference in electron affinity between Co^{4+} (at the surface) and Fe^{3+} (subsurface) sites. Furthermore, adding a W dopant in the vicinity of the Co active site of the Fe-doped CoOOH surface (Fig. 1B, inset) further improves the energetics for OER. The substitution of a W dopant at a Co^{4+} site results in (i) migration of protons away from W, which prefers the W^{6+} formal oxidation state, toward oxygen at Co sites, and (ii) compressive strain of larger W atoms on the surrounding Co sites. As a result of these geometric and electronic changes, we identified a fa-

vorable direct O_2 mechanism for OER with a theoretical overpotential of only 0.4 V compared to the standard electrochemical OOH mechanism [details are provided in (19), computational methodology].

In light of these findings, we sought to devise a controlled process to incorporate W^{6+} into FeCo oxy-hydroxides in an atomically homogeneous manner. We explored a room-temperature sol-gel procedure that would feature precursors mixed in a homogeneous manner that would be hydrolyzed at a controlled rate to achieve atomic homogeneity. First, we dissolved inorganic metal chloride precursors in ethanol. These were controllably hydrolyzed to produce a multimetal oxy-hydroxide gel via a room-temperature sol-gel process (Fig. 2A) (21). The hydrolysis rates of $CoCl_2$, $FeCl_3$ and WCl_6 vary greatly, so very low concentrations of water and propylene oxide were used to tune their hydrolysis independently, a strategy that we anticipated could lead to the desired homogeneous spatial distribution of the three metallic elements (19).

After supercritical drying with CO_2, the gel transformed into an amorphous metal oxy-hydroxide powder. From inductively coupled plasma optical emission spectrometry (ICP-OES) analysis, we determined the molar ratio of Fe:Co:W to be 1:1.02:0.70. Atomic-resolution scanning transmission electron microscopy (STEM) performed in high angle annular dark field (HAADF) mode (Fig. 2D and fig. S5A), combined with selected-area electron diffraction (SAED) analysis (Fig. 2C), revealed the absence of a crystalline phase. X-ray diffraction (XRD) (fig. S2A) further confirmed that the gelled FeCoW is an amorphous phase (19). The STEM measurements show a crumpled and entangled structure composed of nanosheets and nanopores (Fig. 2B). Electron energy loss spectroscopy (EELS) elemental maps with sub-nanometer resolution (Fig. 2E) showed a uniform, uncorrelated spatial distribution of Fe, Co, and W. The statistics of the atom-pair separation distances, obtained from the STEM elemental maps, show that the nearest-neighbor separations of all two-metal atom pairs are highly consistent (fig. S3 - S4, and fig. S6A-E) (19). This homogeneity results from (i) the homogeneous dispersion of three precursors in solution and (ii) controlled hydrolysis, the latter enabling the maintenance of the homogeneous phase in the final gel state without phase separation of different metals caused by precipitation. In contrast, conventional processes (17), even when their precursors are homogeneously mixed, result in crystalline products formed heterogeneously from the liquid phase, leading to phase separation caused by lattice mismatch. For structural comparison with prior sol-gel reports that used an annealing step (17), we annealed the samples at 500°C, and then found crystalline phases (HRTEM images fig. S5B, XRD fig. S2B) that included separated Fe_3O_4, Co_3O_4 and $CoWO_4$. Elemental mapping of this sample (fig. S6 A1-

E1) further confirmed the phase separation of Fe from Co and W atoms (Supplementary Material (*19*)).

We investigated the influence of incorporating W (with its high oxidation state) on the electronic and coordination structures of Fe and Co using x-ray absorption spectroscopy (XAS). We examined (i) conventional layered double hydroxides of FeCo (LDH FeCo) that have the same structure as the state-of-art OER catalysts (LDH NiFe) (*22*); (ii) FeCo oxy-hydroxides (without W) prepared via the annealing-free sol-gel process (gelled FeCo, labeled G-FeCo); (iii) gelled FeCoW oxy-hydroxides (G-FeCoW); and (iv) annealed G-FeCoW at 500°C (A-FeCoW).

To evaluate the change of oxidation states of metal elements during OER, we performed XAS on G-FeCoW and A-FeCoW samples before and after OER; the latter condition is realized by oxidizing samples at +1.4 V versus the reversible hydrogen electrode (RHE) in the OER region. XAS in total electron yield (TEY) mode provides information on the near-surface chemistry (below 10 nm). We acquired TEY data at the Fe and Co L-edges on samples prepared ex situ. For comparison, on the same samples we also measured in situ XAS (i.e., during OER) at the Fe and Co K-edges via fluorescent yield, a measurement that mainly probes chemical changes in the bulk. TEY XAS spectra in Fig. 3A revealed that the surface Fe^{2+} ions in G-FeCoW had been oxidized to Fe^{3+} at +1.4 V, in agreement with thermodynamic data for Fe. However, the oxidation states of Co in G-FeCoW and A-FeCoW samples were appreciably different at 1.4 V. In G-FeCoW, the valence states of both surface (Fig. 3B) and bulk (Fig. 3C) Co were similar to pure Co^{3+}, including only a modest admixture with Co^{2+} (fig. S12): in particular, the Co-K edge profile closely resembled CoOOH (*23*), consistent with our DFT model. In contrast, in A-FeCoW (in which W is phase-separated), even after a potential of 1.4 V is applied, the surface (Fig. 3B) and bulk (Fig. 3C) manifested a substantially higher Co^{2+} content (fig. S12), consistent with the Co_3O_4 and $CoWO_4$ phases. These oxides had been found to be much less reactive in DFT simulations (*14, 20*). The bulk and surface Fe and Co edges profiles were shown in fig. S7-S11 and discussed in Supplementary Material (*19*).

The white lines of W L_3-edge XANES spectra of all samples in Fig. 3D show that W in G-FeCoW and A-FeCoW samples before and after OER has a distorted WO_6 octahedral symmetry (*24*). The W L_3 amplitude in pre-OER A-FeCoW was low, a finding attributable to the loss of bound water during annealing (*24*). When a +1.4 V bias was applied, the W L_3 intensity in G-FeCoW increased, indicating that the valence of W decreases, consistent with increased distortion of WO_6 octahedra (*24*). This result agrees with the results of DFT wherein W-doped CoOOH(01-12) is expected to produce W residing in a lower oxidation state. These results indicate that Fe and Co also inversely influence W in the homogeneous ternary metal oxy-hydroxides.

In situ extended x-ray absorption fine structure (EXAFS) (see fig. S13-14) on G-FeCoW showed a significant decrease in Co-O bond distance, from 2.06 to 1.91 Å after a potential of 1.4 V was applied. This decrease is consistent with the reported results that the Co-O bond distance in CoOOH is shorter than that in $Co(OH)_2$ (*23*). EXAFS data at the Fe edge in G-FeCoW show the same trend (see fig. S15-16). Ex situ EXAFS data before OER are also shown in fig. S17-20 and Table S3. In contrast, the local structural arrangement in A-FeCoW remains unchanged at 1.4 V. Overall, we conclude that Co in the G-FeCoW structure is more readily oxidized to high valence, consistent with G-FeCoW being more active than the control annealed samples.

We compared the OER performance of our gelled sample G-FeCoW with that of the reference samples G-FeCo, LDH FeCo and A-FeCoW. Representative OER currents of the samples were measured for spin-coated thin films (thickness ~ 30 nm, fig. S21) (*19*) on a well-defined Au(111) single-crystal electrode (Fig. 4A) in 1 M KOH aqueous electrolyte at a scan rate of 1 mV s^{-1} (currents are uncorrected and thus include the effects of resistive losses incurred within the electrolyte). The G-FeCoW-on-Au(111) required an overpotential of only 315 mV at 10 mA cm^{-2} (Table 1, all current densities based on projected geometric area). This potential is 114 mV lower than that of precipitated FeCo LDH fabricated for the present study. When W was not introduced, the resultant G-FeCo gelled catalyst required an additional overpotential of 31 mV to reach a similar current density. When the gelled sample was subjected to a postsynthetic thermal treatment (500°C anneal), the overpotential of the FeCoW electrode increased to 405 mV at 10 mA cm^{-2}.

To assess the impact of the electrode support and compare the performance of the new catalysts with state-of-art NiFeOOH, we tested on glass carbon electrode (GCE) using the identical three-electrode system and with a catalyst loading mass of 0.21 mg cm^{-2}. The trend of the overpotentials remains the same (Fig. S22), with the G-FeCoW-on-GCE electrode requiring an overpotential of 223 mV at 10 mA cm^{-2}. Without carbon additives, and without *iR* corrections, the G-FeCoW catalyst consistently outperforms the best oxide catalysts previously reported (Table 1) (*4, 22, 25*).

Next we investigated whether the OER-performance of G-FeCoW originates from intrinsic catalytic activity of multimetal active sites or exclusively from an enhanced surface area. We analyzed the Brunauer-Emmett-Teller (BET) surface area, which allowed us to report normalized kinetic current density (referred to as specific activity) as a function of potential versus RHE (*7*). We confirmed that the intrinsic activity of G-FeCoW is notably higher than that of the controls, and also higher than those previously reported (fig. S26) (*7*).

The intrinsic activity of G-FeCoW was further confirmed by determining the mass activities and turnover frequency (TOFs) for this catalyst. We used data obtained on GCE with 95% iR correction at η = 300 mV (Note: unless otherwise stated, remaining data in this work are not corrected by 95% iR). As shown in Table 1 and tables S5 and S9 (19), the G-FeCoW catalysts on GCE exhibit TOFs of 0.46 s^{-1} per total 3d metal atoms and mass activities of 1175 A g^{-1} (considering the total loading mass on the lower limiting case). If only considering electrochemically active 3d metals or mass (obtained from the integration of Co redox features) (26), G-FeCoW catalysts exhibit a much higher TOFs of 1.5 s^{-1} and 3500 A g^{-1}. These are > three times above the TOF and mass activities of the optimized control catalysts and the repeated the state-of-art NiFeOOH (table S9) (5, 26).

To assess the kinetic barriers involved in OER, we studied the effect of temperature on the performance of the catalysts (fig. S27). OER proceeds more rapidly at elevated temperatures, reflecting the exponential temperature dependence of the chemical rate constant (27). The Arrhenius plots at η = 300 mV for four different catalysts (Fig. 4D) allowed us to extract electrochemical activation energies that agree well with values reported previously (Table 1) (27). We found that G-FeCoW has the lowest apparent barrier value of 49 kJ mol^{-1}. The similar data obtained for all catalysts suggests that OER proceeds via the same potential-determining step on all catalysts investigated herein.

To obtain a highly efficient catalytic electrode, we increased the conductivity of the substrate by loading our catalysts on a nickel foam that was covered with gold to avoid any spurious effects arising from interaction of the catalyst with Ni. The activity trends of catalysts remained the same as observed on the Au(111) surface and GCE, while the absolute performance of each sample was substantially improved (Fig. 4B). The G-FeCoW showed a low overpotential of 191 mV at 10 mA cm^{-2} on the gold-plated nickel foam (projected geometric area, Table 1). Based on the above discussion and the overpotentials on Au(111), gold foam, GCE, and FTO (Fig. 4C, fig. S30, and table S6), it can be seen that the catalytic activity of G-FeCoW is much higher than that of the annealed control (A-FeCoW), gelled FeCo without W (G-FeCo), and the LDH FeCo having the same structure as the state-of-art LDH NiFeOOH OER catalysts.

The operating stability of the OER catalysts is essential to their application (28). To characterize the performance stability of the G-FeCoW catalysts, we ran water oxidation on the catalyst deposited on gold-plated Ni foam under constant current of 30 mA cm^{-2} continuously for 550 hours. We observed no appreciable increase in potential in this time interval (Fig. 4, E and F). To check that the catalyst remained physically intact, we tested in situ its mass using the electrochemical crystal microbalance (EQCM) technique

(fig. S31-32), and also assessed whether any metal had leached into the electrolyte using inductively coupled plasma atomic emission spectroscopy (ICP-AES, fig. S33-36, table S7). Following the completion of an initial burn-in period in which (presumably unbound) W is shed into the electrolyte, we saw stable operation, and no discernible W loss. EELS mapping of G-FeCoW after OER (fig. S37) indicates that the remaining W continues to be distributed homogeneously in the sample. By measuring the O$_2$ evolved from the G-FeCoW/gold-plated Ni foam catalyst, we also confirmed the high activity throughout the entire duration of stability test, obtaining quantitative (i.e., unity Faradaic efficiency) gas evolution of O$_2$ to within our available +/− 5% experimental error (Fig. 4F). These findings suggest that modulating the 3d transition in metal oxy-hydroxides using a suitable transition metal, one closely atomically coupled through homogeneous solid-state dispersion, may provide further avenues to OER optimization.

REFERENCES AND NOTES

1. C. R. Cox, J. Z. Lee, D. G. Nocera, T. Buonassisi, Ten-percent solar-to-fuel conversion with nonprecious materials. *Proc. Natl. Acad. Sci. U.S.A.* **111**, 14057–14061 (2014). Medline doi:10.1073/pnas.1414290111
2. J. Luo, J. H. Im, M. T. Mayer, M. Schreier, M. K. Nazeeruddin, N. G. Park, S. D. Tilley, H. J. Fan, M. Grätzel, Water photolysis at 12.3% efficiency via perovskite photovoltaics and Earth-abundant catalysts. *Science* **345**, 1593–1596 (2014). Medline doi:10.1126/science.1258307
3. M. Schreier *et al.*, *Nat. Commun.* (2015). 10.1038/ncomms8326
4. R. D. L. Smith, M. S. Prévot, R. D. Fagan, Z. Zhang, P. A. Sedach, M. K. Siu, S. Trudel, C. P. Berlinguette, Photochemical route for accessing amorphous metal oxide materials for water oxidation catalysis. *Science* **340**, 60–63 (2013). Medline doi:10.1126/science.1233638
5. D. Friebel, M. W. Louie, M. Bajdich, K. E. Sanwald, Y. Cai, A. M. Wise, M. J. Cheng, D. Sokaras, T. C. Weng, R. Alonso-Mori, R. C. Davis, J. R. Bargar, J. K. Nørskov, A. Nilsson, A. T. Bell, Identification of highly active Fe sites in (Ni,Fe)OOH for electrocatalytic water splitting. *J. Am. Chem. Soc.* **137**, 1305–1313 (2015). Medline doi:10.1021/ja511559d
6. M. W. Kanan, D. G. Nocera, In situ formation of an oxygen-evolving catalyst in neutral water containing phosphate and Co2+. *Science* **321**, 1072–1075 (2008). Medline doi:10.1126/science.1162018
7. J. Suntivich, K. J. May, H. A. Gasteiger, J. B. Goodenough, Y. Shao-Horn, A perovskite oxide optimized for oxygen evolution catalysis from molecular orbital principles. *Science* **334**, 1383–1385 (2011). Medline doi:10.1126/science.1212858
8. A. Vojvodic, J. K. Nørskov, Chemistry. Optimizing perovskites for the water-splitting reaction. *Science* **334**, 1355–1356 (2011). Medline
9. Q. Yin, J. M. Tan, C. Besson, Y. V. Geletii, D. G. Musaev, A. E. Kuznetsov, Z. Luo, K. I. Hardcastle, C. L. Hill, A fast soluble carbon-free molecular water oxidation catalyst based on abundant metals. *Science* **328**, 342–345 (2010). Medline doi:10.1126/science.1185372
10. M. Dincă, Y. Surendranath, D. G. Nocera, Nickel-borate oxygen-evolving catalyst that functions under benign conditions. *Proc. Natl. Acad. Sci. U.S.A.* **107**, 10337–10341 (2010). Medline doi:10.1073/pnas.1001859107
11. F. M. Toma, A. Sartorel, M. Iurlo, M. Carraro, P. Parisse, C. Maccato, S. Rapino, B. R. Gonzalez, H. Amenitsch, T. Da Ros, L. Casalis, A. Goldoni, M. Marcaccio, G. Scorrano, G. Scoles, F. Paolucci, M. Prato, M. Bonchio, Efficient water oxidation at carbon nanotube-polyoxometalate electrocatalytic interfaces. *Nat. Chem.* **2**, 826–831 (2010). Medline doi:10.1038/nchem.761
12. M. S. Burke, M. G. Kast, L. Trotochaud, A. M. Smith, S. W. Boettcher, Cobalt-iron (oxy)hydroxide oxygen evolution electrocatalysts: The role of structure and composition on activity, stability, and mechanism. *J. Am. Chem. Soc.* **137**, 3638–

3648 (2015). Medline

13. M. W. Louie, A. T. Bell, An investigation of thin-film Ni-Fe oxide catalysts for the electrochemical evolution of oxygen. *J. Am. Chem. Soc.* **135**, 12329–12337 (2013). Medline doi:10.1021/ja405351s

14. M. Bajdich, M. García-Mota, A. Vojvodic, J. K. Nørskov, A. T. Bell, Theoretical investigation of the activity of cobalt oxides for the electrochemical oxidation of water. *J. Am. Chem. Soc.* **135**, 13521–13530 (2013). Medline doi:10.1021/ja405997s

15. C. C. L. McCrory, S. Jung, I. M. Ferrer, S. M. Chatman, J. C. Peters, T. F. Jaramillo, Benchmarking hydrogen evolving reaction and oxygen evolving reaction electrocatalysts for solar water splitting devices. *J. Am. Chem. Soc.* **137**, 4347–4357 (2015). Medline doi:10.1021/ja510442p

16. J. A. Haber *et al.*, Energy. *Environ. Sci.* **7**, 682 (2014).

17. J. A. Haber, E. Anzenburg, J. Yano, C. Kisielowski, J. M. Gregoire, *Adv. Ener. Mat.* **5**, 1402307 (2015).

18. P. Liao, J. A. Keith, E. A. Carter, Water oxidation on pure and doped hematite (0001) surfaces: Prediction of Co and Ni as effective dopants for electrocatalysis. *J. Am. Chem. Soc.* **134**, 13296–13309 (2012). Medline doi:10.1021/ja301567f

19. Materials and methods are available as supplementary materials on *Science* Online.

20. C. Ling, L. Q. Zhou, H. Jia, First-principles study of crystalline CoWO4 as oxygen evolution reaction catalyst. *RSC Advances* **4**, 24692 (2014). doi:10.1039/c4ra03893b

21. V. Augustyn, J. Come, M. A. Lowe, J. W. Kim, P. L. Taberna, S. H. Tolbert, H. D. Abruña, P. Simon, B. Dunn, High-rate electrochemical energy storage through Li+ intercalation pseudocapacitance. *Nat. Mater.* **12**, 518–522 (2013). Medline doi:10.1038/nmat3601

22. W. Ma, R. Ma, C. Wang, J. Liang, X. Liu, K. Zhou, T. Sasaki, A superlattice of alternately stacked Ni-Fe hydroxide nanosheets and graphene for efficient splitting of water. *ACS Nano* **9**, 1977–1984 (2015). Medline doi:10.1021/nn5069836

23. R. Subbaraman, D. Tripkovic, K. C. Chang, D. Strmcnik, A. P. Paulikas, P. Hirunsit, M. Chan, J. Greeley, V. Stamenkovic, N. M. Markovic, Trends in activity for the water electrolyser reactions on 3d M(Ni,Co,Fe,Mn) hydr(oxy)oxide catalysts. *Nat. Mater.* **11**, 550–557 (2012). Medline doi:10.1038/nmat3313

24. A. Balerna, E. Bernieri, E. Burattini, A. Kuzmin, A. Lusis, J. Purans, P. Cikmach, XANES studies of MeO3-x (Me = W, Re, Ir) crystalline and amorphous oxides. *Nucl. Instrum. Methods Phys. Res. A* **308**, 240–242 (1991). doi:10.1016/0168-9002(91)90637-6

25. F. Song, X. Hu, *Nat. Commun.* (2014). 10.1038/ncomms5477

26. A. S. Batchellor, S. W. Boettcher, Pulse-Electrodeposited Ni–Fe (Oxy)hydroxide Oxygen Evolution Electrocatalysts with High Geometric and Intrinsic Activities at Large Mass Loadings. *ACS Catalysis* **5**, 6680–6689 (2015). doi:10.1021/acscatal.5b01551

27. J. R. Swierk, S. Klaus, L. Trotochaud, A. T. Bell, T. D. Tilley, Electrochemical Study of the Energetics of the Oxygen Evolution Reaction at Nickel Iron (Oxy)Hydroxide Catalysts. *J. Phys. Chem. C* **119**, 19022–19029 (2015). doi:10.1021/acs.jpcc.5b05861

28. N. Danilovic *et al.*, *Angew. Chem. Int. Ed.*, n/a (2014).

29. F. Rosalbino, S. Delsante, G. Borzone, G. Scavino, *Int. J. Hydrogen Energy* **38**, 10170 (2013).

30. D. Friebel, M. Bajdich, B. S. Yeo, M. W. Louie, D. J. Miller, H. Sanchez Casalongue, F. Mbuga, T. C. Weng, D. Nordlund, D. Sokaras, R. Alonso-Mori, A. T. Bell, A. Nilsson, On the chemical state of Co oxide electrocatalysts during alkaline water splitting. *Phys. Chem. Chem. Phys.* **15**, 17460–17467 (2013). Medline doi:10.1039/c3cp52981a

31. P. E. Blöchl, Projector augmented-wave method. *Phys. Rev. B Condens. Matter* **50**, 17953–17979 (1994). Medline doi:10.1103/PhysRevB.50.17953

32. G. Kresse, D. Joubert, From ultrasoft pseudopotentials to the projector augmented-wave method. *Phys. Rev. B* **59**, 1758–1775 (1999). doi:10.1103/PhysRevB.59.1758

33. J. P. Perdew, K. Burke, M. Ernzerhof, Generalized Gradient Approximation Made Simple. *Phys. Rev. Lett.* **77**, 3865–3868 (1996). Medline doi:10.1103/PhysRevLett.77.3865

34. J. P. Perdew, K. Burke, M. Ernzerhof, Generalized Gradient Approximation Made Simple [Phys. Rev. Lett. 77, 3865 (1996)]. *Phys. Rev. Lett.* **78**, 1396–1396 (1997). Medline doi:10.1103/PhysRevLett.78.1396

35. G. Kresse, J. Furthmüller, Efficiency of ab-initio total energy calculations for metals and semiconductors using a plane-wave basis set. *Comput. Mater. Sci.* **6**, 15–50 (1996). 10.1016/0927-0256(96)00008-0 doi:10.1016/0927-0256(96)00008-0

36. G. Kresse, J. Hafner, Ab initio molecular dynamics for liquid metals. *Phys. Rev. B Condens. Matter* **47**, 558–561 (1993). Medline doi:10.1103/PhysRevB.47.558

37. S. L. Dudarev, G. A. Botton, S. Y. Savrasov, C. J. Humphreys, A. P. Sutton, Electron-energy-loss spectra and the structural stability of nickel oxide: An LSDA+U study. *Phys. Rev. B* **57**, 1505–1509 (1998). doi:10.1103/PhysRevB.57.1505

38. L. Wang, T. Maxisch, G. Ceder, Oxidation energies of transition metal oxides within the GGA + U framework. *Phys. Rev. B* **73**, 195107 (2006). doi:10.1103/PhysRevB.73.195107

39. A. Jain, G. Hautier, S. P. Ong, C. J. Moore, C. C. Fischer, K. A. Persson, G. Ceder, Formation enthalpies by mixing GGA and GGA + U calculations. *Phys. Rev. B* **84**, 045115 (2011). doi:10.1103/PhysRevB.84.045115

40. H. J. Monkhorst, J. D. Pack, Special points for Brillouin-zone integrations. *Phys. Rev. B* **13**, 5188–5192 (1976). doi:10.1103/PhysRevB.13.5188

41. J. Rossmeisl, A. Logadottir, J. K. Nørskov, Electrolysis of water on (oxidized) metal surfaces. *Chem. Phys.* **319**, 178–184 (2005). 10.1016/j.chemphys.2005.05.038 doi:10.1016/j.chemphys.2005.05.038

42. F. Studt, F. Abild-Pedersen, H. A. Hansen, I. C. Man, J. Rossmeisl, T. Bligaard, Volcano Relation for the Deacon Process over Transition-Metal Oxides. *ChemCatChem* **2**, 98–102 (2010). 10.1002/cctc.200900194 doi:10.1002/cctc.200900194

43. Y.-H. Fang, Z.-P. Liu, Mechanism and Tafel lines of electro-oxidation of water to oxygen on RuO2(110). *J. Am. Chem. Soc.* **132**, 18214–18222 (2010). 10.1021/ja1069272 Medline doi:10.1021/ja1069272

44. J. K. Nørskov, J. Rossmeisl, A. Logadottir, L. Lindqvist, J. R. Kitchin, T. Bligaard, H. Jónsson, Origin of the Overpotential for Oxygen Reduction at a Fuel-Cell Cathode. *J. Phys. Chem. B* **108**, 17886–17892 (2004). 10.1021/jp047349j doi:10.1021/jp047349j

45. R. Ma, J. Liang, K. Takada, T. Sasaki, Topochemical synthesis of Co-Fe layered double hydroxides at varied Fe/Co ratios: Unique intercalation of triiodide and its profound effect. *J. Am. Chem. Soc.* **133**, 613–620 (2011). 10.1021/ja1087216 Medline doi:10.1021/ja1087216

46. D. R. Lide, Ed., *Handbook of Chemistry and Physics* (CRC, ed. 78, 1998).

47. V. Stamenković, T. J. Schmidt, P. N. Ross, N. M. Marković, Surface Composition Effects in Electrocatalysis: Kinetics of Oxygen Reduction on Well-Defined Pt3Ni and Pt3Co Alloy Surfaces. *J. Phys. Chem. B* **106**, 11970–11979 (2002). 10.1021/jp021182h doi:10.1021/jp021182h

48. A. B. Anderson, J. Roques, S. Mukerjee, V. S. Murthi, N. M. Markovic, V. Stamenkovic, Activation energies for oxygen reduction on platinum alloys: Theory and experiment. *J. Phys. Chem. B* **109**, 1198–1203 (2005). 10.1021/jp047468z Medline doi:10.1021/jp047468z

49. L. Trotochaud, S. L. Young, J. K. Ranney, S. W. Boettcher, Nickel-iron oxyhydroxide oxygen-evolution electrocatalysts: The role of intentional and incidental iron incorporation. *J. Am. Chem. Soc.* **136**, 6744–6753 (2014). 10.1021/ja502379c Medline doi:10.1021/ja502379c

50. M. S. Burke, L. J. Enman, A. S. Batchellor, S. Zou, S. W. Boettcher, Oxygen Evolution Reaction Electrocatalysis on Transition Metal Oxides and (Oxy)hydroxides: Activity Trends and Design Principles. *Chem. Mater.* **27**, 7549–7558 (2015). 10.1021/acs.chemmater.5b03148 doi:10.1021/acs.chemmater.5b03148

51. M. S. Burke, S. Zou, L. J. Enman, J. E. Kellon, C. A. Gabor, E. Pledger, S. W. Boettcher, Revised Oxygen Evolution Reaction Activity Trends for First-Row Transition-Metal (Oxy)hydroxides in Alkaline Media. *J. Phys. Chem. Lett.* **6**, 3737–3742 (2015). 10.1021/acs.jpclett.5b01650 Medline doi:10.1021/acs.jpclett.5b01650

52. S. Jung, C. C. L. McCrory, I. M. Ferrer, J. C. Peters, T. F. Jaramillo, Benchmarking nanoparticulate metal oxide electrocatalysts for the alkaline water oxidation reaction. *J. Mater. Chem. A* **4**, 3068–3076 (2016). 10.1039/c5ta07586f

doi:10.1039/C5TA07586F

53. M. Gong, Y. Li, H. Wang, Y. Liang, J. Z. Wu, J. Zhou, J. Wang, T. Regier, F. Wei, H. Dai, An advanced Ni-Fe layered double hydroxide electrocatalyst for water oxidation. *J. Am. Chem. Soc.* **135**, 8452–8455 (2013). 10.1021/ja4027715 Medline doi:10.1021/ja4027715

54. J. Huang, J. Chen, T. Yao, J. He, S. Jiang, Z. Sun, Q. Liu, W. Cheng, F. Hu, Y. Jiang, Z. Pan, S. Wei, CoOOH Nanosheets with High Mass Activity for Water Oxidation. *Angew. Chem. Int. Ed. Engl.* **54**, 8722–8727 (2015). 10.1002/anie.201502836 Medline doi:10.1002/anie.201502836

55. A. J. Esswein, Y. Surendranath, S. Y. Reece, D. G. Nocera, Highly active cobalt phosphate and borate based oxygen evolving catalysts operating in neutral and natural waters. *Energy Environ. Sci.* **4**, 499–504 (2011). 10.1039/c0ee00518e doi:10.1039/C0EE00518F

56. H. Wang, H. W. Lee, Y. Deng, Z. Lu, P. C. Hsu, Y. Liu, D. Lin, Y. Cui, Bifunctional non-noble metal oxide nanoparticle electrocatalysts through lithium-induced conversion for overall water splitting. *Nat. Commun.* **6**, 7261 (2015). 10.1038/ncomms8261 Medline doi:10.1038/ncomms8261

ACKNOWLEDGMENTS

SUPPLEMENTARY MATERIALS

www.sciencemag.org/cgi/content/full/science.aaf1525/DC1
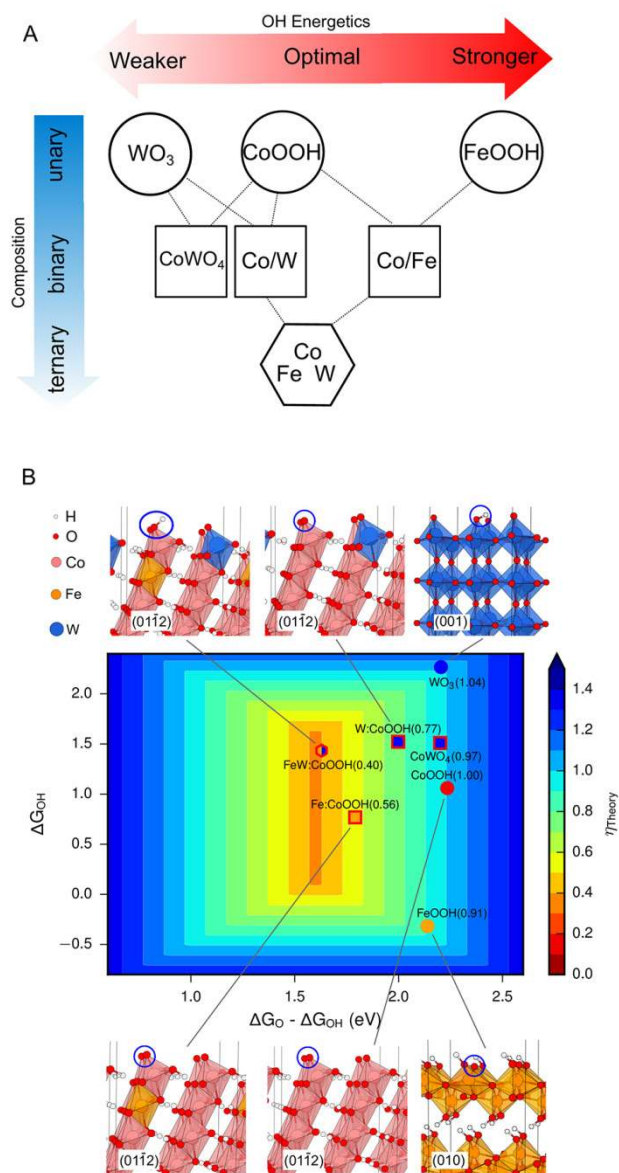Materials and Methods
Figs. S1 to S43
Table S1 and S9
References (*31–56*)

23 December 2015; accepted 9 March 2016
Published online 24 March 2016
10.1126/science.aaf1525

Fig. 1. Fig. 1. Tuning the energetics of OER intermediates via alloying. (A) Change in adsorption energetics (ΔG_{OH}) as function of increasing composition obtained by interpolation between calculated pure phases: WO_3 (001), $CoOOH$ (01-12), $FeOOH$ (010) and $CoWO_4$ (010) (20). (B) DFT+U calculated OER activities of pure and W-doped CoFe oxy-hydroxides and W oxides. The optimum is obtained for WFe-doped β-CoOOH (see also Table S1 for details). The insets show the optimized structures and location of dopants and active sites at potential limiting step. For DFT+U methodology and detailed information about these systems please refer to Supplementary Material.
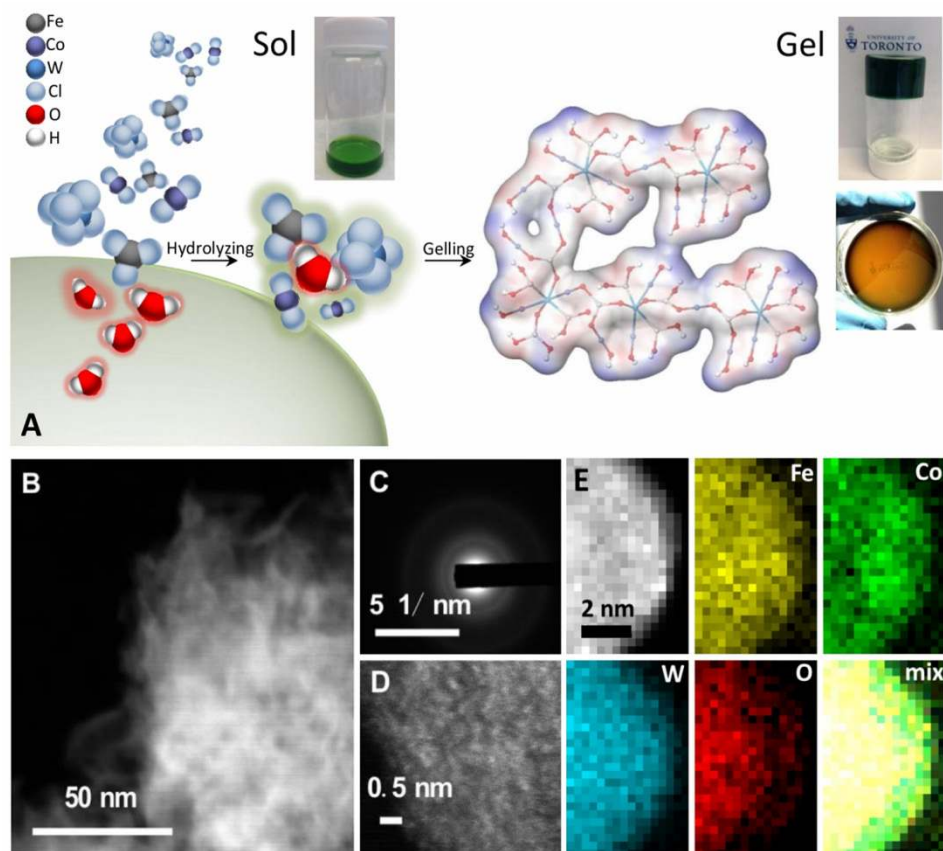
Fig. 2. Fig. 2. Preparation of G-FeCoW oxy-hydroxides catalysts. (**A**) Schematic illustration of preparation process for the gelled structure and pictures of corresponding sol, gel and gelled film. (**B**) High-angle-annular-dark-field (HAADF) STEM image of nanoporous structure of G-FeCoW. (**C**) Selected area electron diffraction (SAED) pattern. (**D**) Atomic-resolution HAADF-STEM image. (**E**) Electron energy loss spectroscopy (EELS) elemental mapping from G-FeCoW oxy-hydroxide sample.
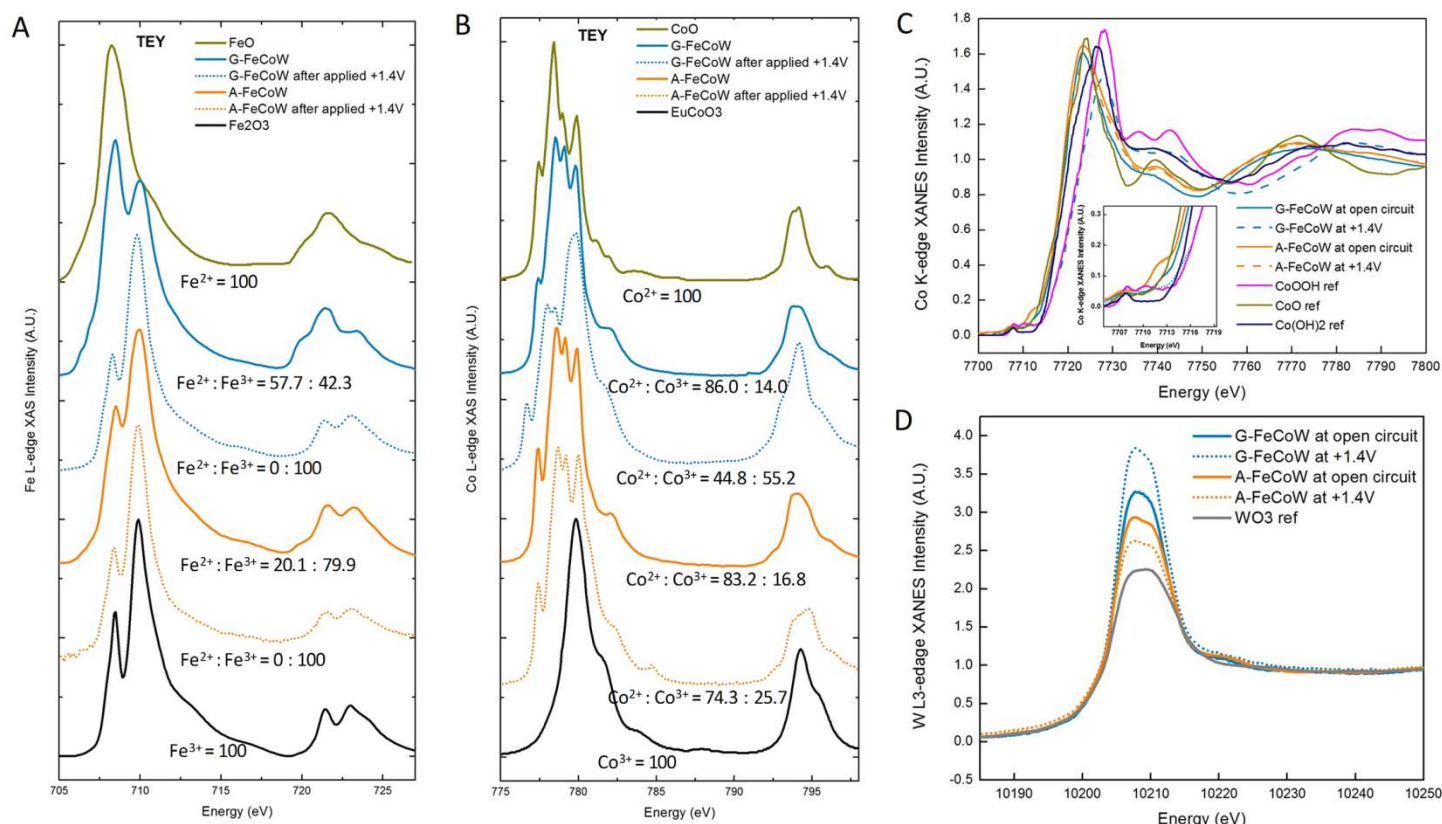
Fig. 3. Fig. 3. Surface and bulk X-ray absorption spectra of G-FeCoW oxy-hydroxides catalysts and A-FeCoW controls. (**A**) Surface sensitive TEY XAS scans at the Fe L-edge before and after OER at +1.4 V (vs. RHE), with the corresponding molar ratio of Fe^{2+} and Fe^{3+} species. (**B**) Surface sensitive TEY XAS scans at the Co L-edge before and after OER at +1.4 V (vs. RHE). (**C**) Bulk Co K-edge XANES spectra before and after OER at +1.4 V (vs. RHE); Inset is the zoomed in pre-edge profiles; The Co K-edge data of $Co(OH)_2$ and CoOOH are from (*30*). (**D**) Bulk W L3-edge XANES spectra before and after OER at +1.4 V (vs. RHE).
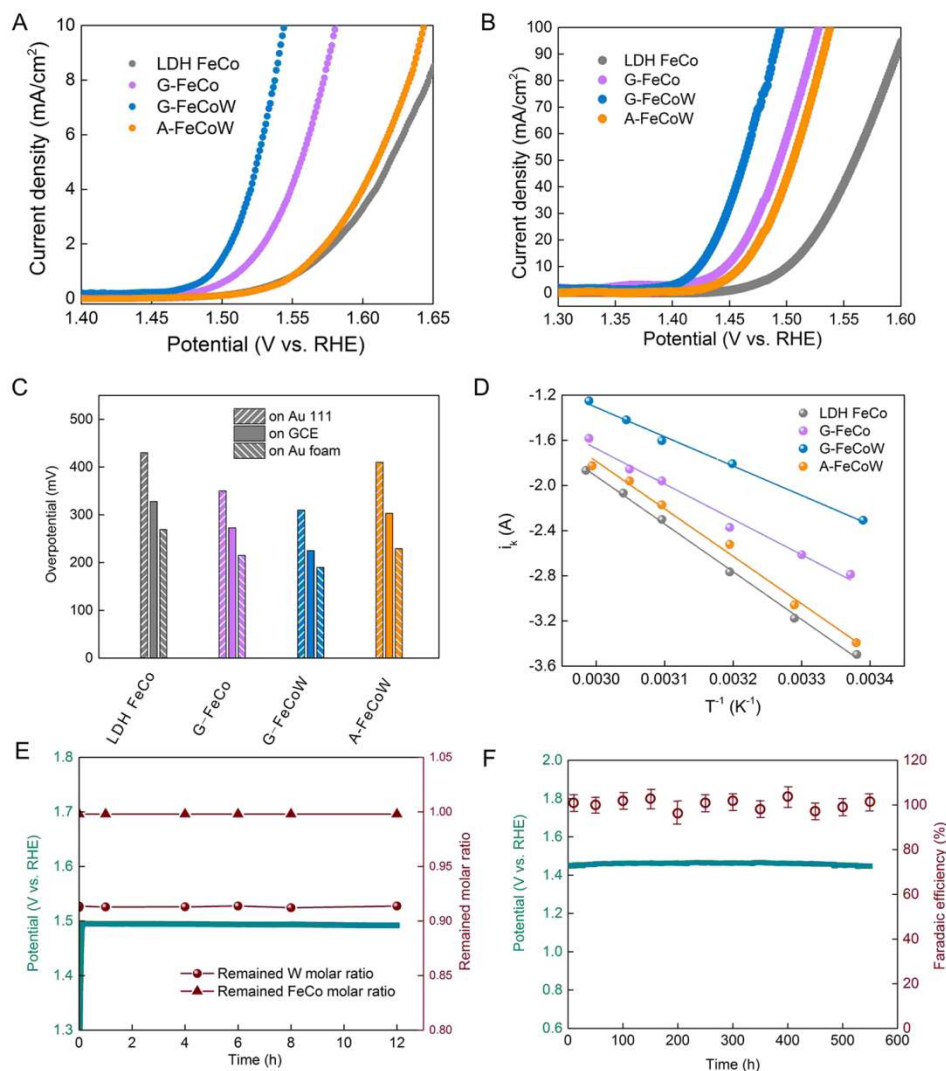
Fig. 4. Fig. 4. Performance of G-FeCoW oxy-hydroxide catalysts and controls in three-electrode configuration in 1 M KOH aqueous electrolyte. The OER polarization curve of catalysts loaded on two different substrates with 1 mV s^{-1} scan rate, without *iR*-correction: (A) Au(111) electrode; (B) gold-plated Ni foam. (C) Overpotentials obtained from OER ploarization curves at the current density of 10 mA cm^{-2} tested on Au(111), glass carbon and gold-plated Ni foam, respectively, without *iR*-correction. (D) Arrhenius plot of the kinetic current at η = 300 mV, tested on Au(111), without *iR*-correction. (E) Chronopotentiometric curves obtained with the G-FeCoW oxy-hydroxides on gold-plated Ni foam electrode with constant current densities of 30 mA cm^{-2}, and the corresponding remaining metal molar ratio in G-FeCoW calculated from ICP-AES results. (F) Chronopotentiometric curves obtained with the G-FeCoW oxy-hydroxides on gold-plated Ni foam electrode with constant current densities of 30 mA cm^{-2}, and the corresponding Faradaic efficiency from gas chromatography measurement of evolved O$_2$.

Table 1. Comparison of catalytic parameters of gelled FeCoW and controls.

Samples	On gold foam Overpotential* (mV)	On glass carbon Overpotential* (mV)	TOF† (s^{-1})	On Au(111) Overpotential* (mV)	ΔH (kJ mol^{-1}) at η=300 mV	Reference
LDH FeCo	279 (-/+8)	331 (-/+3)	0.0085	429 (-/+4)	81	This work
Gelled-FeCo	215 (-/+6)	277 (-/+3)	0.043	346 (-/+4)	60	This work
Gelled-FeCoW	191 (-/+3)	223 (-/+2)	0.46 (-/+0.08)	315 (-/+5)	49	This work
Annealed-FeCoW	232 (-/+4)	301 (-/+4)	0.17	405 (-/+2)	80	This work
Amorphous-FeCoO$_x$‡	–	300	–	–	–	(4)
LDH NiFe	–	300	0.07	–	–	(25)
CoOOH	–	–	–	550	–	(23)
IrO$_2$	–	260	0.05	–	–	(25)
NiFeOOH	–	340	–	–	66 (-/+5)	(27)
Ni$_{60}$Co$_{40}$ oxides	–	263	–	–	72.6§	(29)
NiFe LDH/ GO	–	210	0.1	–	–	(22)

*Obtained at the current density of 10 mA cm^{-2}, without *iR*-correction.
†Obtained at 95% *iR*-corrected overpotential = 300 mV, assuming all loaded 3d-metal atoms as active sites.
‡Obtained from the LSV plots at the current density of 4 mA cm^{-2} in 0.1 M KOH aqueous solution.
§Obtained at 280 mV in 1M NaOH aqueous solution.